I&EC research
Industrial & Engineering Chemistry Research

Article

pubs.acs.org/IECR

Combined Ceria Reduction and Methane Reforming in a Solar-Driven Particle-Transport Reactor

Michael Welte,[†] Kent Warren,[‡] Jonathan R. Scheffe,*[,‡] and Aldo Steinfeld*[,†]

[†]Department of Mechanical and Process Engineering, ETH Zürich, 8092 Zürich, Switzerland
[‡]Department of Mechanical and Aerospace Engineering, University of Florida, Gainesville, Florida 32611-6250, United States

ABSTRACT: We report on the experimental performance of a solar aerosol reactor for carrying out the combined thermochemical reduction of CeO_2 and reforming of CH_4 using concentrated radiation as the source of process heat. The 2 kW_{th} solar reactor prototype utilizes a cavity receiver enclosing a vertical Al_2O_3 tube which contains a downward gravity-driven particle flow of ceria particles, either co-current or counter-current to a CH_4 flow. Experimentation under a peak radiative flux of 2264 suns yielded methane conversions up to 89% at 1300 °C for residence times under 1 s. The maximum extent of ceria reduction, given by the nonstoichiometry δ ($CeO_{2-\delta}$), was 0.25. The solar-to-fuel energy conversion efficiency reached 12%. The syngas produced had a H_2:CO molar ratio of 2, and its calorific value was solar-upgraded by 24% over that of the CH_4 reformed.

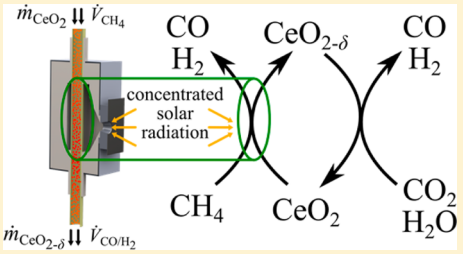

1. INTRODUCTION

Thermochemical redox cycles driven by concentrated solar energy are a promising route to split H_2O and CO_2 and produce syngas,[1,2] a mixture of H_2 and CO that can be further processed to liquid hydrocarbon fuels via established gas-to-liquid processes. Nonstoichiometric ceria is currently considered the state of the art among nonvolatile redox materials because of its rapid kinetics and crystallographic stability.[3−6] The two-step cycle comprises the endothermic reduction of ceria generally operated at above 1400 °C, followed by the lower-temperature exothermic reoxidation of ceria to its initial state with H_2O and CO_2 to form syngas. Various solar reactor concepts have been proposed for effecting this cycle, some of them experimentally demonstrated, including packed beds,[7,8] porous structures,[9−13] rotating components,[14−16] and moving particles,[17−20] that incorporated heat recovery during the temperature-swing mode or operated under isothermal mode. An intriguing approach to decrease the reduction temperature and thus the temperature swing between reduction and oxidation is to combine this redox cycle with the reforming of methane,[21,22] according to the following:

Reduction-Reforming:

$$CeO_2 + \delta CH_4 \rightarrow CeO_{2-\delta} + \delta(CO + 2H_2) \quad (1)$$

Oxidation with CO_2/H_2O:

$$CeO_{2-\delta} + \delta CO_2 \rightarrow CeO_2 + \delta CO \quad (2a)$$

$$CeO_{2-\delta} + \delta H_2O \rightarrow CeO_2 + \delta H_2 \quad (2b)$$

During the endothermic reduction step (eq 1), CeO_2 is reduced in the presence of CH_4 to an extent given by the nonstoichiometry δ, where the required high-temperature heat is delivered by concentrated solar energy. The δ moles of oxygen released from the ceria partially oxidize CH_4 to form CO and H_2. In the subsequent exothermic oxidation step (eq 2), $CeO_{2-\delta}$ reacts with CO_2 or H_2O to reincorporate oxygen into the lattice and form additional CO or H_2, respectively. Reactions 2a and 2b intrinsically assume full oxidation at thermodynamically favorable temperatures below 1000 °C.[23,24] Such a combined reduction-reforming processing using concentrated solar heat was previously proposed in the context of the co-production of metals and syngas.[25,26] The introduction of a reducing agent such as CH_4 during the reduction step effectively lowers the oxygen partial pressure and shifts the equilibrium to lower temperatures, below 1000 °C.[21,22] Thus, it enables the operation of the two-step cycle isothermally, as demonstrated with a fixed bed reactor in the range 900−1000 °C.[27] Using a similar fixed bed reactor in the range 400−800 °C, Pt was shown to catalyze the surface-controlled kinetics.[28]

This concept is similar to chemical looping combustion (CLC) or chemical looping reforming (CLR) processes that also utilize metal oxides as an intermediate.[29−34] The main advantage of these concepts compared to direct combustion or reforming is that the fuel and oxidant do not come into direct contact. Thus, in the case of CLC, CO_2 can be generated without dilution in air, and in the case of CLR, high purity H_2[27] or CO may be produced in the oxidation reactor without contamination by trace combustion gases. The main difference to the proposed concept is that, in CLC/CLR, the energy for endothermic reduction of the metal oxide is typically supplied by fuel combustion while the proposed concept aims at utilizing concentrated solar energy as the source of high-temperature process heat. The advantage to using ceria as a redox intermediate

Received: July 6, 2017
Revised: August 18, 2017
Accepted: August 22, 2017
Published: August 22, 2017

DOI: 10.1021/acs.iecr.7b02738
Ind. Eng. Chem. Res. 2017, 56, 10300−10308

compared to other oxides is related to its rapid kinetics, favorable thermodynamics, and selectivity, as discussed in depth by Krenzeke et al.[27] and Warren et al.[22]

Dry reforming and steam reforming of methane driven by solar energy have also been investigated intensively,[35] most recently by Wegeng et al.[36] In contrast, the proposed combined reduction-reforming process does not require the use of catalysts, even for dry reforming. For example, the oxidation of ceria in the presence of CO_2 is known to be totally selective to CO production.[9−11,13] As such, a wide range of synthesis gas ratios ($CO:H_2$ between 1:1 and 1:3) are achievable without the need for a downstream water−gas shifting reactor by co-feeding CO_2 and H_2O during the oxidation step.[11]

We recently proposed a solar particle-transport reactor concept based on a cavity-receiver enclosing an array of alumina tubes, each containing a downward flow of ceria particles counter to an inert sweep gas flow.[17,18] This concept offers in situ separation of the solid and gas products, enhanced heat and mass transfer, good scalability due to the modular tubular configuration, and continuous operation of the reduction step. It further offers the possibility to individually design the (nonsolar) oxidation reactor and operate it independently and round-the-clock in combination with a particle storage. Possible configurations for an oxidation reactor include but are not limited to riser reactors and moving bed reactors. However, because of the indirect heat transfer to the reaction site by conduction through the Al_2O_3 tube and convection−radiation to the particle flow, tube temperatures of 1500 °C and above were required for the effective reduction of ceria particles in short residence times. This critical temperature requirement can be significantly alleviated by the combined reduction-reforming approach.

In this work, we report on the experimental performance of the solar particle-transport reactor for the thermal reduction of ceria particles with CH_4. We study the impact of temperature, ceria particle mass flow rate, gas flow rate, and CH_4 concentration on the extent of ceria reduction, methane conversion, and syngas quality. An energy balance is carried out for each experimental run to determine the solar-to-fuel energy conversion efficiency. We further compare counter-current and co-current gas−particle flow configurations and investigate the reactor stability under steady-state operating conditions.

2. EXPERIMENTAL METHODS

The schematic of the lab-scale solar reactor is shown in Figure 1. It is composed of an Al_2O_3 tube (Haldenwanger, ALSINT 99.7, D_{out} = 52 mm, D_{in} = 40 mm, L = 850 mm) vertically positioned inside a cavity receiver (100 mm × 100 mm × 250 mm). The cavity is lined with 76.2 mm-thick Al_2O_3 insulation (Zircar Zirconia, Type BusterM-35) supported by a 5 mm-thick aluminum shell. High-flux radiation enters the cavity through a polished Al compound parabolic concentrator[37] (CPC, half acceptance angle of 45°) positioned in front of the windowless 30 mm-diameter circular aperture.[38] The incident radiative power is absorbed by internal multiple reflections, resulting in a cavity's apparent absorptivity of 88%, determined by Monte Carlo ray tracing performed with the in-house code VEGAS.[39] Ceria particles (Chempur, 99.9% purity, D_{v50} = 40 μm) contained in a 2 kg reservoir were delivered to the alumina tube by means of a screw feeder with adjustable rotational speed and subsequently carried to the reaction zone by gravity. The feeder design limited the particle mass flow rate to 0.6 g s^{-1} to enable reasonable dispersion and avoid severe fluctuations. A balance (Kern FKB 6L0.02, uncertainty < ±0.02 g) below the reaction

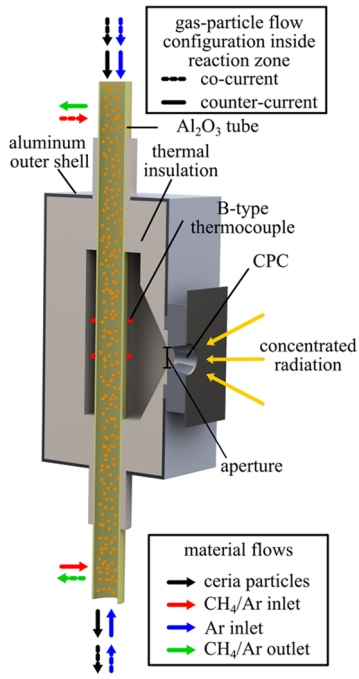

Figure 1. Schematic of the solar particle-transport reactor. Material flows are indicated by the colored arrows for either co-current (dashed) or counter-current (solid) flow configuration.

zone at the exit of the tube enabled online measurements of the mass flow rate of reduced ceria particles $\dot{m}_{CeO_{2-\delta}}$. Electric mass flow controllers (Bronkhorst, F-201C, uncertainty < ±2%) were used to deliver Ar purge gas to the balance housing at the bottom and the feeder at the top. Additionally, two lateral gas connections above and below the reaction zone were implemented to obtain either a co-current or counter-current gas−particle flow through the reaction zone (material flows for both configurations indicated in Figure 1). The product gas composition was analyzed by infrared-based detectors (Siemens Ultramat 6, uncertainty < ±1%) for $CO/CO_2/CH_4$, a paramagnetic alternating pressure O_2 detector (Siemens Oxymat 6, uncertainty < ±1%) and a thermal conductivity-based H_2 detector (Siemens Calomat 6) and validated with gas chromatography (Varian 490, uncertainty < ±1%) measuring H_2, O_2, CO, CO_2, and CH_4. Undetectable species H_2O and C were calculated though molar balances of the supplied CH_4 and measured product gases. The tube temperature distribution was measured on the outside by six shielded thermocouples type-B (uncertainty <0.25%); the average yielded the nominal tube temperature T_{tube}. The temperature distribution of particles, the loading distribution of particles, and the velocity distribution of particles across the radius were not measured. These measurements are complex and require optical techniques to avoid interference with the flow, but optical access was not possible with this solar reactor configuration. Prior to each experimental run, the particles were exposed to air at 300 °C for more than 8 h to ensure a fully oxidized state (δ_i = 0). Carbon contamination in the ceria particles was below 0.004 $mol_C\ mol_{CeO_2}^{-1}$, as also verified by thermogravimetric analysis in air at 800 °C.

The experiments were carried out at the high-flux solar simulator (HFSS) of ETH Zurich. An array of seven Xe-arcs, close-coupled to truncated ellipsoidal reflectors, provided an external source of intense thermal radiation, mostly in the visible and infrared spectra, that closely approximated the heat transfer

DOI: 10.1021/acs.iecr.7b02738
Ind. Eng. Chem. Res. 2017, 56, 10300−10308

characteristics of highly concentrating solar systems such as towers and dishes.[40] The radiative flux distribution at the aperture plane was measured with a calibrated CCD camera focused on a refrigerated Al_2O_3 plasma-coated Lambertian (diffusely reflecting) target. The total solar radiative power input P_{solar} at the exit of the CPC was calculated by flux integration and verified by water calorimetry.

During a typical experimental run, the cavity receiver was heated by concentrated radiation to the desired T_{tube} in the range of 1150−1350 °C, while being purged with Ar to reduce the oxygen partial pressure below 200 ppmv. Once steady-state T_{tube} was reached, P_{solar} was maintained within 1.1−1.6 kW for mean solar concentration ratios of 1556−2264 suns (1 sun = 1 kW m^{-2}). Ar purge flows of 0.5 and 1 L_N min^{-1} (SLPM, gas flow rates calculated at 273.15 K and 1 atm) were delivered to the feeder and the balance housing, respectively. An Ar/CH4 gas mixture was delivered to the lateral gas inlet at variable flow rates and concentrations to obtain the desired flow conditions in the reaction zone. Typical Re numbers of the gas flow were in the range 25−40, indicative of laminar regime. The CH_4 concentration was limited to 10% because of lab safety regulations.

3. RESULTS AND DISCUSSION

Representative Experiment. Figure 2 shows the variation of the ceria mass flow rate (left axis) and CH_4 inlet molar flow

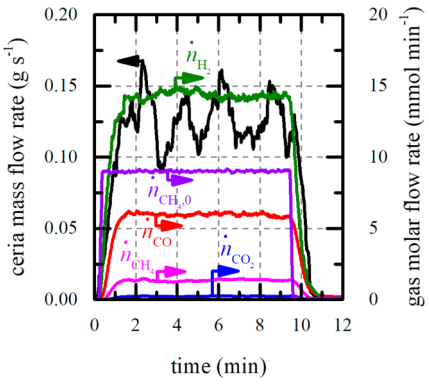

Figure 2. Ceria mass flow rate at average $\dot{m}_{CeO_2}$ = 0.13 g s^{-1} ($\dot{n}_{CeO_2}$ = 44.2 mmol min^{-1}) (left axis) and CH_4 inlet/outlet, H_2, CO, and CO_2 molar flow rates (right axis) as a function of time during a representative experimental run. The subscript 0 indicates the inlet condition. Experimental conditions: T_{tube} = 1302 °C, δ_{final} = 0.16, $\dot{V}_{CH_4/Ar}$ = 2 L_N min^{-1}, co-current flow configuration.

rate (right axis) alongside H_2, CO, CO_2, and CH_4 outlet molar flow rates as a function of time during a representative experimental run. In this run, $\dot{m}_{CeO_2}$ = 0.13 g s^{-1} ($\dot{n}_{CeO_2}$ = 44.2 mmol min^{-1}) of ceria particles were fed for 9.5 min with a $\dot{V}_{CH_4/Ar}$ = 2 L_N min^{-1} flow of 10% CH_4−Ar ($\dot{n}_{CH_4}$ = 9.0 mmol min^{-1}) through the reaction zone at a constant T_{tube} of 1303 °C. After a short stabilization period, outlet flows of H_2, CO, CO_2, and unreacted CH_4 reached steady-state even though $\dot{m}_{CeO_2}$ fluctuated due to poor dispersion by the particle screw feeder. $\dot{m}_{CeO_2}$ was calculated by $\dot{m}_{CeO_2} = \dot{m}_{CeO_{2-\delta}} + M_O(\dot{n}_{CO} + 2\dot{n}_{CO_2} + \dot{n}_{H_2O})$, where $\dot{m}_{CeO_{2-\delta}}$ is the mass flow rate of reduced ceria (online balance measurement), M_O denotes the molar mass of monatomic oxygen, and $\dot{n}_i$ denotes the molar flow rate of species i (GC and feed gas flows measurements). During steady-state $\dot{n}_{H_2}$ = 14 mmol min^{-1}, $\dot{n}_{CO}$ = 6 mmol min^{-1}, $\dot{n}_{CO_2}$ = 0.24 mmol min^{-1}, $\dot{n}_{H_2O}$ = 0.75 mmol min^{-1}, $\dot{n}_C$ = 1.2 mmol min^{-1}, and $\dot{n}_{CH_4}$ = 1.4 mmol min^{-1}. The final nonstoichiometry, $\delta_{final} = (\dot{n}_{CO} + 2\dot{n}_{CO_2} + \dot{n}_{H_2O})/\dot{n}_{CeO_2}$, was 0.16. The methane conversion, $X_{CH_4} = 1 - \dot{n}_{CH_4}/\dot{n}_{CH_{4,0}}$, was 0.85.

Effect of Ceria Mass Flow Rate. The effect of $\dot{m}_{CeO_2}$ on δ_{final} at T_{tube} = 1302 °C, $\dot{V}_{CH_4/Ar}$ = 2 L_N min^{-1}, and $x_{CH_{4,0}}$ = 0.1 is shown in Figure 3a and b by filled squares for co-current and counter-current gas−particle flows, respectively. For both gas−particle flow configurations, δ_{final} decreased with increasing $\dot{m}_{CeO_2}$. Additionally, for the same $\dot{m}_{CeO_2}$, counter-current flow resulted in a higher δ_{final}. For example, for $\dot{m}_{CeO_2}$ = 0.13g s^{-1}, δ_{final} was 0.18 and 0.23 for co-current and counter-current gas−particle flow, respectively. For the investigated temperature range, a closed-system thermodynamic analysis[22] indicates that, at equilibrium, δ_{eq} approaches the stoichiometric ratio $\delta_{eq} \approx \dot{n}_{CH_{4,0}}/\dot{n}_{CeO_2}$. δ_{eq} is plotted in Figure 3a and b by the dashed red line. Interestingly, $\delta_{final} > \delta_{eq}$ for $\dot{m}_{CeO_2}$ > 0.2 g s^{-1} with the co-current flow configuration and for all $\dot{m}_{CeO_2}$ with the counter-current flow configuration. This apparent inconsistency is explained by comparing the measured product composition with the thermodynamic equilibrium composition. Figure 4a displays the equilibrium composition and corresponding ceria nonstoichiometry δ_{eq} for the system CeO_2 + 0.25CH_4 as a function of temperature at 1 atm. Computations were carried out following the methodology outlined in Warren et al.[21] and considered the following species: CeO_2, CH_4, H_2, CO, CO_2, C, and O_2. For n_{i,CH_4} = 0.25 mol_{CH_4} $mol_{CeO_2}^{-1}$, δ_{eq} increases with temperature until 1027 °C where it plateaus due to the complete CH_4 conversion. Below this temperature, C formation derived from CH_4 decomposition is thermodynamically favorable. Above this temperature, a shift from C to CO occurs as oxygen evolves from ceria. Syngas constitutes more than 99 mol % of the products at equilibrium with molar ratio H_2/CO approaching 2. H_2O and CO_2 are minimal throughout the considered temperature span. Figure 4b evaluates the impact of syngas for initial molar fractions corresponding to the complete CH_4 conversion (n_{i,H_2} = 0.5 mol_{H2} $mol_{CeO_2}^{-1}$ and $n_{i,CO}$ = 0.25 mol_{CO} $mol_{CeO_2}^{-1}$) on the ceria nonsoichiometry. Similar to Figure 4a, δ_{eq} increases with temperature. However, in the absence of CH_4, the gas composition contains increasing amounts of H_2O and CO_2. Additionally, for a given temperature, δ_{eq} is lower for reduction with syngas compared to that with CH_4. Consequently, in the presence of CH_4 (Figure 4a), no further reduction of ceria with products H_2 and CO is possible in a closed system.

The measured product composition is plotted in Figure 5a and b for the co-current and counter-current flow configurations, respectively. For both configurations, x_{H_2} decreased and x_{H_2O} increased with increasing $\dot{m}_{CeO_2}$, while all other molar fractions remained relatively constant. This shift from H_2 to H_2O, which is more accentuated under the counter-current gas flow configuration, contradicts the thermodynamic prediction (Figure 4a). The formation of water is attributed to the reduction of ceria with H_2, which is thermodynamically favorable in the absence of CH_4 (Figure 4b). Thus, we hypothesize that ceria is reduced initially by H_2 and then by CH_4 to an extent larger than δ_{eq}. For the co-current flow configuration,

DOI: 10.1021/acs.iecr.7b02738
Ind. Eng. Chem. Res. 2017, 56, 10300−10308

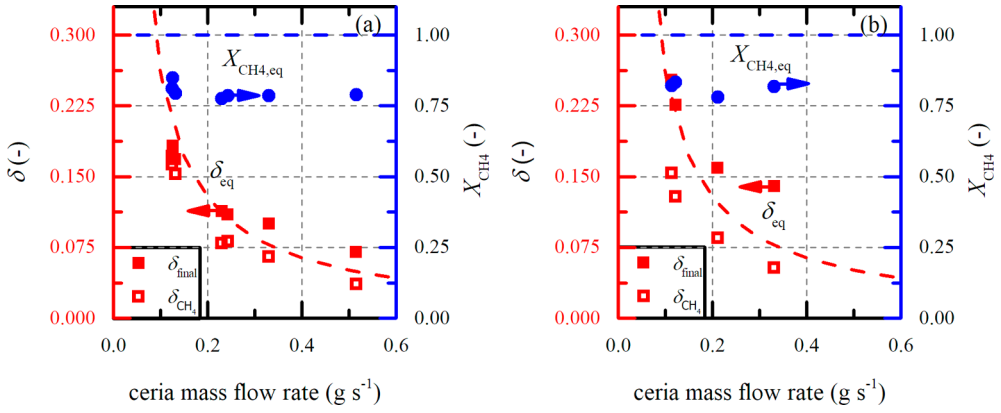

Figure 3. Nonstoichiometry δ_{final} (closed symbols) and δ_{CH_4} (open symbols) alongside CH_4 conversion as a function of ceria mass flow rate for the co-current (a) and counter-current (b) flow configurations. δ_{eq} and $X_{CH_4,eq}$, indicated by the dashed curves, correspond to thermodynamic equilibrium solutions for a closed system. Experimental conditions: T_{tube} = 1302 °C, $\dot{V}_{CH_4/Ar}$ = 2 L_N min^{-1}, $x_{CH_4,0}$ = 0.1.

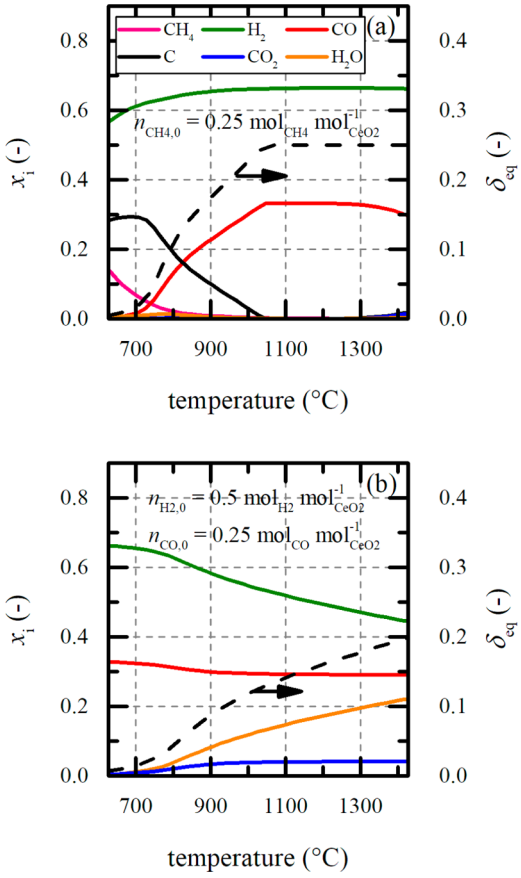

Figure 4. Equilibrium composition and corresponding ceria nonstoichiometry as a function of temperature for the following systems: (a) CeO_2 + 0.25CH_4 and (b) CeO_2 + 0.5H_2 + 0.25CO.

this is only possible if H_2 diffuses counter to the gas flow, which can be expected because of a low Peclet number of 0.77. For the counter-current flow configuration, unreduced ceria inherently comes in contact with produced syngas, resulting in a higher value of δ_{final} at the same $\dot{m}_{CeO_2}$ as well as a stronger decrease in x_{H2} with increasing $\dot{m}_{CeO_2}$. We recognize that δ_{final} as defined previously is a superposition of the influence of different reducing species, namely, CH_4, H_2, and CO, and thus can be divided into their respective influence according to

$$\delta_{final} = \overbrace{\frac{\dot{n}_{CO} + \dot{n}_{CO_2}}{\dot{n}_{CeO_2}}}^{\delta_{CH_4}} + \overbrace{\frac{\dot{n}_{CO_2}}{\dot{n}_{CeO_2}}}^{\delta_{CO}} + \overbrace{\frac{\dot{n}_{H_2O}}{\dot{n}_{CeO_2}}}^{\delta_{H_2}} \quad (3)$$

δ_{CH_4} isolates the nonstoichiometry resulting from the reduction with methane without considering the additional reducing agents H_2 and CO, and thus $\delta_{CH_4} \leq \delta_{eq}$. δ_{CH4} is plotted in Figure 3a and b by the open red squares and closely follows the trend of δ_{eq} for both flow configurations. Both configurations result in the same δ_{CH_4} for a given mass flow rate and consequently equal X_{CH4}. This indicates that the reaction is not kinetically limited. The gain obtained in δ_{final} by operating with counter-current flow configuration is a result of undesired reactions between ceria and product syngas. While the consumed syngas is regained during a subsequent oxidation step, these side reactions result in dilution of the product syngas with H_2O and CO_2, requiring energy intensive postprocessing. Consequently, the co-current gas particle flow configuration is considered to be superior and will be the focus of further investigation.

Effect of Tube Temperature. Figure 6a shows the impact of the nominal temperature of the Al_2O_3 tube on ceria nonstoichiometry (left axis) and corresponding methane conversion (right axis) for a ceria mass flow rate of $\dot{m}_{CeO_2}$ = 0.13 g s^{-1}, gas flow of $\dot{V}_{CH_4/Ar}$ = 2 L_N min^{-1}, inlet methane concentration of 10%, and co-current gas−particle flow. As T_{tube} was raised from 1150 to 1350 °C, δ_{final} increased from 0.025 to 0.22, respectively, and X_{CH_4} increased from 0.39 to 0.89, respectively. With similar nonstoichiometries of 0.2 and 0.25, however, lower X_{CH_4} of 0.6 and 0.52 were obtained in packed bed reactors at ceria temperatures of 1000 and 1120 °C, respectively.[22,27] This points to a significant difference between the measured tube wall temperature and the actual particle temperature. Similar to the results shown in Figure 3, δ_{final} exceeds the predicted closed system equilibrium (dashed line), presumably due to the reaction of ceria particles with product gases H_2 and CO at T_{tube} = 1350 °C. All syngas consumed in this manner during the reduction step is reformed during the oxidation step and, consequently, results in no additional gain/loss in fuel yield. The uncertainty in δ_{final} is estimated to be below 10% based on the standard deviation of measurements taken for 1250 and 1300 °C

DOI: 10.1021/acs.iecr.7b02738
Ind. Eng. Chem. Res. 2017, 56, 10300−10308

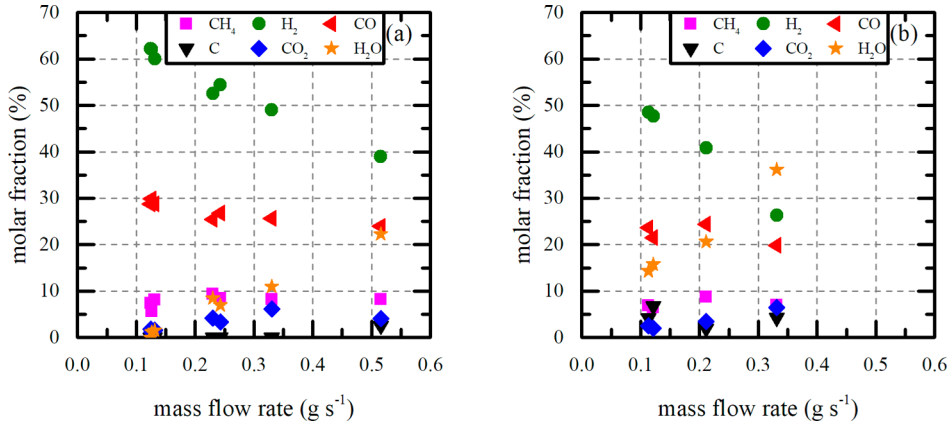

Figure 5. Product composition as a function of ceria mass flow rate for the co-current (a) and counter-current (b) flow configurations (Ar is omitted). Experimental conditions: T_{tube} = 1302 °C, $\dot{V}_{CH_4/Ar}$ = 2 L_N min^{-1}, $x_{CH_{4,0}}$ = 0.1.

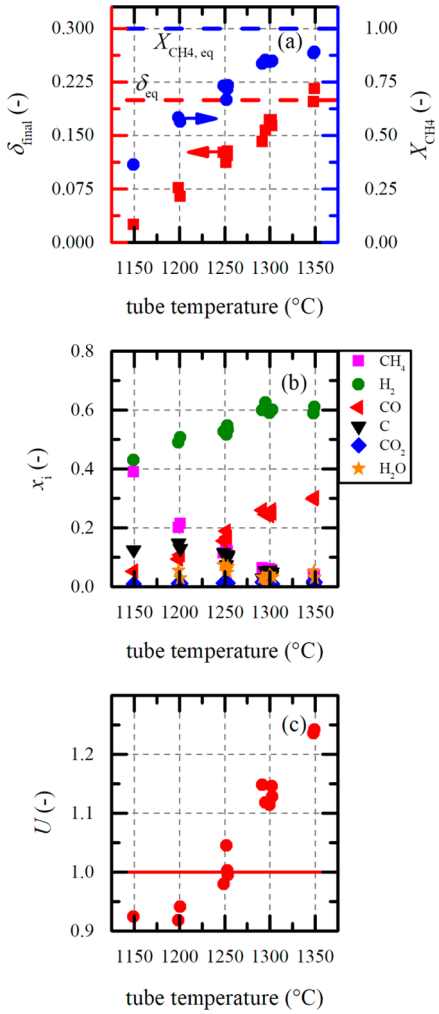

Figure 6. (a) Nonstoichiometry and methane conversion as a function of the nominal temperature of the Al_2O_3 tube and the corresponding equilibrium values δ_{eq} and $X_{CH_{4,eq}}$. (b) Corresponding product compositions (Ar is omitted). (c) Corresponding upgrade factor. Experimental conditions: $\dot{m}_{CeO_2}$ = 0.13 g s^{-1}, $\dot{V}_{CH_4/Ar}$ = 2 L_N min^{-1}, $x_{CH_{4,0}}$ = 0.1, co-current flow configuration.

on consecutive days (Figure 6). It is mainly due to fluctuations in the ceria mass flow rate with time, as shown in Figure 2. These fluctuations are inherent to the feeder design and can be as high as ±30% of the average mass flow rate delivered during steady-state operation. This high extent of ceria reduction and CH_4 conversion was realized in very short particle residence times (<1 s) inherent to the present lab-scale reactor. Since complete conversion is thermodynamically favorable at the investigated temperatures. For example, at a methane to ceria ratio of 0.25, complete conversion is favorable at 1000 °C as indicated in Figure 4; thermodynamic limitations were not expected at tube temperatures above 1300 °C. Equilibrium curves for δ_{eq} and $X_{CH_{4,eq}}$ are indicated in Figure 6a. Figure 6b shows the molar fraction of product species, $x_i = \dot{n}_i/\dot{n}_{tot}$, where $\dot{n}_{tot}$ corresponds to the sum of all molar flows except Ar but including unmeasured C and H_2O. As expected, both x_{H_2} and x_{CO} increased with T_{tube}, while x_{CH_4} decreased, yielding at 1350 °C a H_2:CO molar ratio of 2, suitable for gas-to-liquid processing via Fischer–Tropsch. Trace amounts of CO_2 and H_2O were indicative of the high selectivity from CH_4 to syngas. Formation of solid carbon, attributed to CH_4 cracking on hot nucleation surfaces (tube walls and ceria particles), reached a maximum solid phase molar fraction of x_C = 0.13 at 1150 °C but was eliminated at above 1300 °C.

The upgrade factor U is defined as ratio of the energy contained in the outlet flow to the energy content of the inlet flow, given by

$$U = \frac{\dot{n}_{H_2} HV_{H_2} + \dot{n}_{CO} HV_{CO} + \dot{n}_{CeO_2} \delta_{final} HV_{CO} + \dot{n}_{CH_4} HV_{CH_4}}{\dot{n}_{CH_4,0} HV_{CH_4}} \quad (4)$$

where HV_i corresponds to the (high) heating value of species i. This definition intrinsically assumes complete reoxidation of ceria with CO_2. Note that the energy content of carbon deposited is not considered because it is an undesirable product. U increased from 0.92 to 1.2 when T_{tube} was raised from 1150 °C 1350 °C, as shown in Figure 6c. At T_{tube} < 1250 °C, U < 1 partly because of carbon deposition. At T_{tube} > 1250 °C, U > 1 which indicates solar energy stored in the form of syngas. For comparison, U < 0.92 for autothermal steam-based reforming of methane without the involvement of ceria, fueled by combustion of excess methane.

Effect of Gas Flow Rate. Figure 7a shows δ_{final} and X_{CH_4} as a function of the CH_4/Ar gas flow rate while keeping $x_{CH4,0}$ = 0.1, T_{tube} = 1300 °C, and $\dot{m}_{CeO_2}$ = 0.14 g s^{-1} and for the

DOI: 10.1021/acs.iecr.7b02738
Ind. Eng. Chem. Res. 2017, 56, 10300−10308

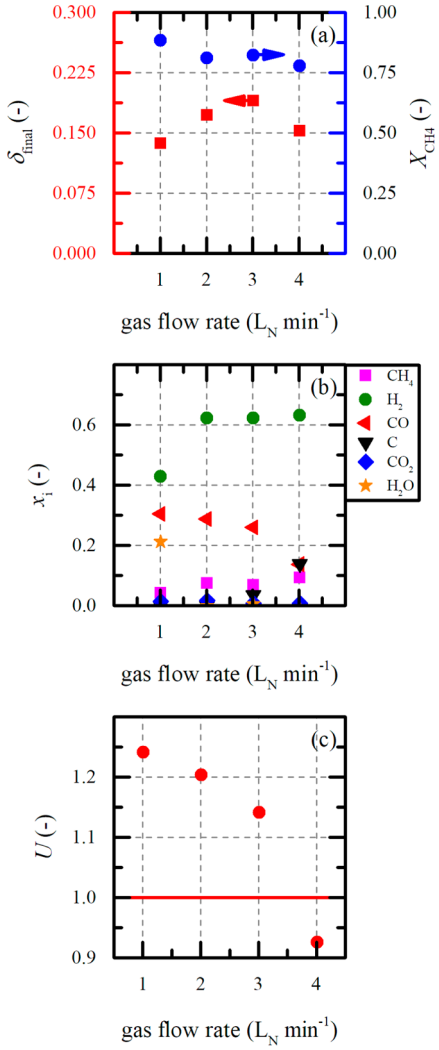

Figure 7. (a) Nonstoichiometry and CH_4 conversion as a function of the gas flow rate. (b) Corresponding product composition (Ar is omitted). (c) Corresponding upgrade factor. Experimental conditions: T_{tube} = 1302 °C, $\dot{m}_{CeO_2}$ = 0.14 g s^{-1}, $x_{CH_{4,0}}$ = 0.1, co-current flow configuration.

co-current flow configuration. The corresponding product composition is shown in Figure 7b. With increasing $\dot{V}$, the amount of CH_4 available for the reaction increased proportionally, resulting in a peak δ_{final} = 0.19 for $\dot{V}_{CH_4/Ar}$ = 3 L_N min^{-1}. A further increase in $\dot{V}_{CH_4/Ar}$ resulted in a decrease in δ_{final} and x_{CO} due to the carbon formation associated with CH_4 cracking, possibly caused by shorter gas and particle residence times and the resulting heat transfer and kinetic limitations. The residence time limitation is further supported by the decrease in X_{CH_4} with $\dot{V}_{CH_4/Ar}$ shown in Figure 7a. Consequently, U monotonically decreased as well (Figure 7c).

Effect of Methane Concentration. Figure 8a shows δ_{final} and X_{CH_4} as a function of $x_{CH_{4,0}}$ for T_{tube} = 1303 °C, $\dot{m}_{CeO_2}$ = 0.12 g s^{-1}, $\dot{V}_{CH_4/Ar}$ = 2 L_N min^{-1}, and co-current flow configuration. The corresponding product compositions are shown in Figure 8b. δ_{final} increased monotonically from 0.088 to 0.18 when $x_{CH_{4,0}}$ increased from 2.5% to 10%, while X_{CH_4} remained nearly constant at 0.86 ± 0.02 over this range, corresponding to x_{CH_4} = 0.053, presumably due to mass transfer effects in the

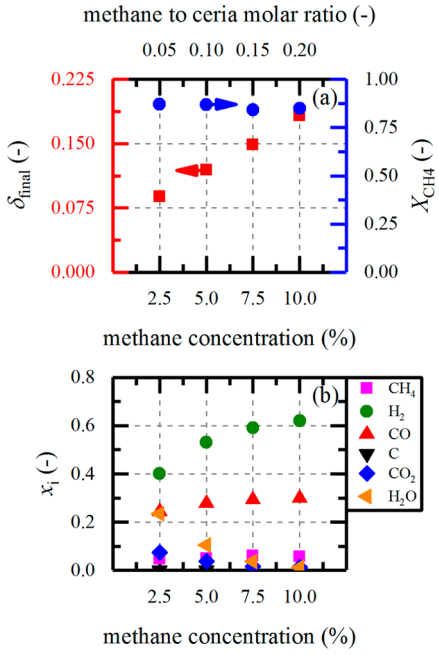

Figure 8. (a) Nonstoichiometry alongside methane conversion for varying inlet methane concentration. (b) Corresponding product composition (Ar is omitted). Experimental conditions: T_{tube} = 1303 °C, $\dot{m}_{CeO_2}$ = 0.12 g s^{-1}, $\dot{V}_{CH_4/Ar}$ = 2 L_N min^{-1}, co-current flow configuration.

co-current flow configuration. x_{H_2} and x_{CO} increased with $x_{CH4,0}$ and correlated with a decrease in x_{H_2O} and x_{CO_2}. It is likely, that the particles reach conditions were the reduction with syngas is thermodynamically favorable for low methane to ceria rations, resulting in increased H_2O and CO_2 formation. Carbon formation was not observed under these conditions, resulting in a constant U = 1.25 ± 0.02.

Solar-to-Fuel Energy Conversion Efficiency. The solar-to-fuel energy conversion efficiency, $\eta_{solar\text{-}to\text{-}fuel}$, is defined as the ratio of the (high) calorific value of syngas (H_2 and CO) produced to the summation of the solar radiative energy input and the calorific value of the converted CH_4. It is thus given by

$$\eta_{solar\text{-}to\text{-}fuel} = \frac{\dot{n}_{H_2} HV_{H_2} + \dot{n}_{CO} HV_{CO} + \dot{n}_{CeO_2} \delta_{final} HV_{CO}}{P_{solar} + (\dot{n}_{CH_4,0} - \dot{n}_{CH_4}) HV_{CH_4}} \quad (5)$$

Note that the third term in the numerator accounts for the energy stored in the reduced ceria; i.e., it assumes that reduced ceria is completely reoxidized with CO_2 (eq 2a) to generate additional CO. The heating value of carbon is not included because it is an undesired byproduct. No energy penalty is accounted for inert gas consumption because Ar dilution was used only for safety lab regulations. $\eta_{solar\text{-}to\text{-}fuel}$ is plotted in Figure 9a–d as a function of T_{tube}, $\dot{m}_{CeO_2}$, $\dot{V}_{CH_4/Ar}$, and $x_{CH_{4,0}}$, respectively. Despite the associated reradiation losses, $\eta_{solar\text{-}to\text{-}fuel}$ increased from 3.2% at 1150 °C to 9.4% at 1350 °C. As expected, $\eta_{solar\text{-}to\text{-}fuel}$ also increased monotonically with $x_{CH_{4,0}}$. In contrast, $\dot{m}_{CeO_2}$ had no significant influence regardless of the flow configuration, yielding $\eta_{solar\text{-}to\text{-}fuel}$ = 8.4 ± 0.4%. $\eta_{solar\text{-}to\text{-}fuel}$ increased with $\dot{V}$ peaked at 12% for $\dot{V}_{CH_4/Ar}$ = 3 L_N min^{-1} and decreased because of solid carbon deposition and residence time limitations. At this point, it is not possible to compare

DOI: 10.1021/acs.iecr.7b02738
Ind. Eng. Chem. Res. 2017, 56, 10300−10308

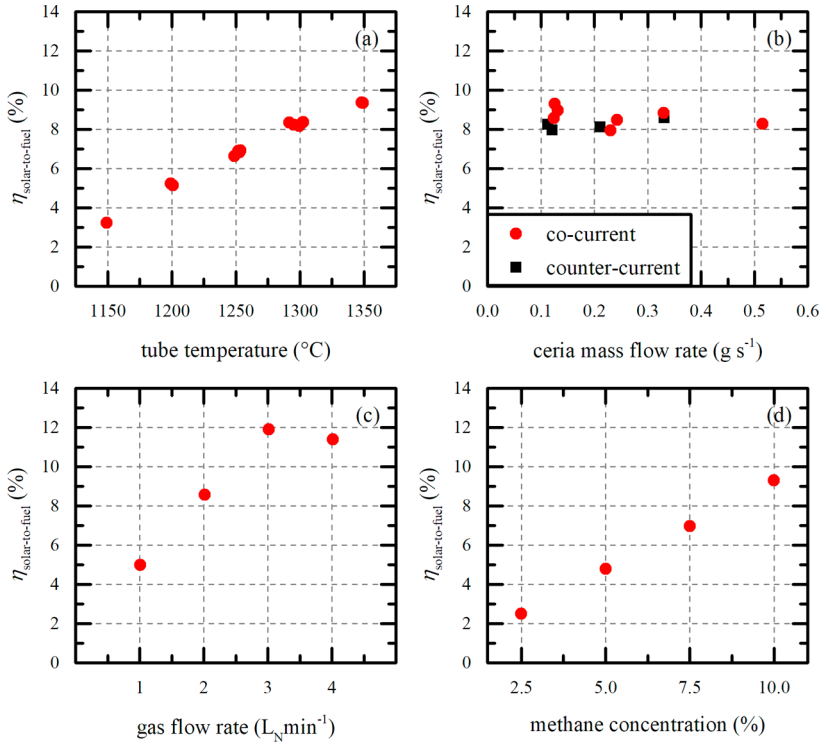

Figure 9. Solar-to-fuel energy conversion efficiency as a function of the nominal temperature of the Al_2O_3 tube (a), ceria mass flow rate (b), gas flow rate (c), and inlet methane concentration (d). Experimental conditions if not stated otherwise in the graph: T_{tube} = 1303 °C, $\dot{m}_{CeO_2}$ = 0.13 g s^{-1}, $\dot{V}_{CH_4/Ar}$ = 2 L_N min^{-1}, $x_{CH_{4,0}}$ = 0.1, co-current flow configuration.

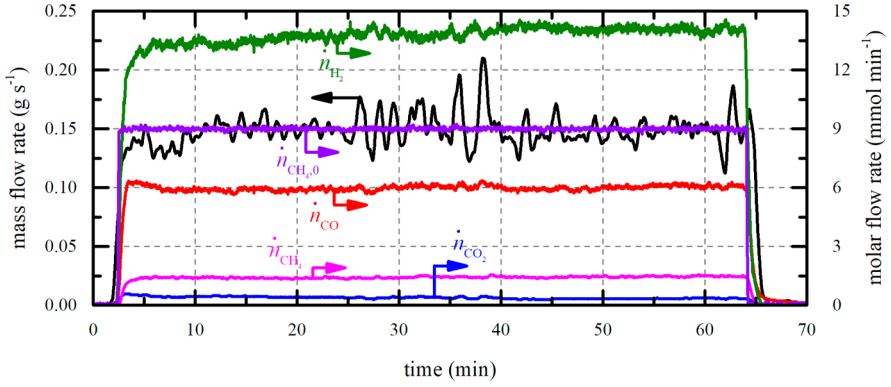

Figure 10. Continuous syngas production for over 60 min with stable outlet gas composition. Experimental conditions: T_{tube} = 1291 °C, δ = 0.15, $\dot{V}_{CH_4/Ar}$ = 2 L_N min^{-1}, $x_{CH_{4,0}}$ = 0.1, mean $\dot{m}_{CeO_2}$ = 0.15 g s^{-1} ($\dot{n}_{CeO_2}$ = 53.7 mmol min^{-1}), co-current flow configuration.

these results directly to other studies in the literature. $\eta_{solar\text{-}to\text{-}fuel}$ would be a relevant indicator to compare, for example, to the value obtained for the solar reforming of methane without ceria ($CH_4 + H_2 \rightarrow 3H_2 + CO$). The PNNL's reforming system,[36] which uses heat exchangers to recover the sensible heat of the hot outlet stream, reports an efficiency of 69% but is defined based on the enthalpy change of the reaction and without considering the calorific value of methane (HV_{CH_4}) as energy input in the denominator, i.e., different definition than eq 5 and thus difficult to compare. Since we are only driving half of the redox cycle without any heat recovery, the particles are heated from ambient to the reaction temperature, affecting detrimentally $\eta_{solar\text{-}to\text{-}fuel}$. In a complete cycle with efficient heat management between reduction and oxidation steps, the particles should enter the reactor near the reaction temperature. To maximize $\eta_{solar\text{-}to\text{-}fuel}$, the reactor should be operated in the upper range of T_{tube}, while $\dot{V}_{CH_4/Ar}$ needs to be selected to maximize the CH_4 supply while avoiding residence time limitations.

Steady-State Syngas Production. Figure 10 shows the continuous syngas production for over 60 min for an experimental run with co-current flow configuration and for T_{tube} = 1291 °C, $\dot{V}_{CH_4/Ar}$ = 2 L_N min^{-1}, $x_{CH_{4,0}}$ = 0.1 ($\dot{n}_{CH_4}$ = 9.03 mmol min^{-1}), and mean $\dot{m}_{CeO_2}$ = 0.15 g s^{-1} ($\dot{n}_{CeO_2}$ = 53.7 mmol min^{-1}). Shortly after the particle feeder and the inlet gas flow were initiated and despite the fluctuation in $\dot{m}_{CeO_2}$, the CO and H_2 flow rates reached steady-state conditions at about 6 and 13.7 mmol min^{-1}, respectively, resulting in a H_2:CO ratio of 2.3. The deviation from 2 is due to trace amounts of CO_2 production (x_{CO_2} = 0.015) and carbon deposition (x_C = 0.029). For this run, X_{CH_4} = 0.85 and $\eta_{solar\text{-}to\text{-}fuel}$ = 8.3%. No evidence of a reaction between ceria particles and the Al_2O_3 tube was observed. Carbon deposition was observed but did not exceed x_C = 0.029 and

DOI: 10.1021/acs.iecr.7b02738
Ind. Eng. Chem. Res. 2017, 56, 10300−10308

may be avoided by operating at above 1300 °C (Figure 3b) and/or by co-feeding H_2O.

4. SUMMARY AND CONCLUSIONS

The technical feasibility of the solar particle-transport reactor was experimentally demonstrated for performing the combined CeO_2 reduction and CH_4 reforming process using both counter-current and co-current flow configurations. Experiments driven by high-flux irradiation resulted in peak $\eta_{solar\text{-}to\text{-}fuel}$ of 12% and an upgrade factor of 14% at T_{tube} = 1303 °C, $\dot{m}_{CeO_2}$ = 0.13 g s^{-1}, $\dot{V}_{CH_4/Ar}$ = 3 L_N min^{-1}, and $x_{CH_{4,0}}$ = 0.1 with a co-current flow configuration. Further, a peak upgrade factor of 24%, $\eta_{solar\text{-}to\text{-}fuel}$ = 9%, and methane conversion of 89% were obtained at T_{tube} = 1303 °C, $\dot{m}_{CeO_2}$ = 0.13 g s^{-1}, $\dot{V}_{CH_4/Ar}$ = 1 L_N min^{-1}, and $x_{CH_{4,0}}$ = 0.1 with a co-current flow configuration.

Ceria nonstoichiometry (reduction extent), efficiency, and methane conversion increased with temperature, while carbon formation was suppressed at tube temperatures above 1300 °C. In contrast, nonstoichiometry decreased with ceria mass flow rate, while efficiency and methane conversion were unaffected. Interestingly, H_2 molar fractions decreased with increasing ceria mass flow rate, while the H_2O molar fractions increased correspondingly. This trend was more pronounced for counter-current flow configuration and was attributed to the reaction of unreacted ceria with the produced syngas. Continuous steady-state operation for over 1 h yielded syngas of quality suitable for gas-to-liquid processing. Reaction kinetics over short residence times are the main limitation at the current scale. We conclude that the solar particle-transport reactor is a robust and scalable concept for effecting the combined CeO_2 reduction and CH_4 reforming process.

AUTHOR INFORMATION

Corresponding Authors

*. E-mail: jscheffe@ufl.edu (J. R. Scheffe).

*. E-mail: aldo.steinfeld@ethz.ch (A. Steinfeld).

ORCID

Michael Welte: 0000-0002-8342-5535

Kent Warren: 0000-0001-7657-0956

Notes

The authors declare no competing financial interest.

ACKNOWLEDGMENTS

We gratefully acknowledge the financial support by the Swiss State Secretariat for Education, Research and Innovation (Grant No. 16.0183), the European Union's Horizon 2020 research and innovation program (Project INSHIP − Grant No. 731287), and the European Research Council under the European Union's ERC Advanced Grant (Project SUNFUELS − Grant No. 320541).

NOMENCLATURE DESCRIPTION

D_{in} = inner tube diameter, m
D_{out} = outer tube diameter, m
D_{v50} = median particle diameter for volume-based distribution, μm
HV_i = (high) heating value of species i, kJ
L = tube length, m
M_i = molar mass of species i, g mol^{-1}
$\dot{m}_{CeO_2}$ = inlet ceria mass flow rate, g s^{-1}
$\dot{m}_{CeO_{2-\delta}}$ = mass flow rate of reduced ceria, g s^{-1}
n_i = molar ratio of species i to ceria, mol_i mol_{CeO2}^{-1}
$\dot{n}_i$ = molar flow rate of species i, mol s^{-1}
$\dot{n}_{tot}$ = total molar flow rate except Argon, mol s^{-1}
P_{solar} = solar radiative power input, kW_{th}
SLPM = standard liters per min, calculated at 273.15 K and 101 325 Pa
T_{tube} = nominal reaction tube temperature, °C
U = upgrade factor
$\dot{V}$ = gas flow rate through reaction zone, L_N min^{-1}
x_i = molar fraction of species i
X_{CH_4} = methane conversion
δ = ceria nonstoichiometry
δ_{eq} = ceria nonstoichiometry at equilibrium
δ_i = initial ceria nonstoichiometry
δ_{final} = final ceria nonstoichiometry
δ_{CH_4} = ceria nonstoichiometry resulting from reaction with CH_4
δ_{CO} = ceria nonstoichiometry resulting from reaction with CO
δ_{H_2} = ceria nonstoichiometry resulting from reaction with H_2
$\eta_{solar\text{-}to\text{-}fuel}$ = solar-to-fuel energy conversion efficiency

REFERENCES

(1) Steinfeld, A. Solar thermochemical production of hydrogen−−a review. *Sol. Energy* **2005**, *78*, 603−615.

(2) Smestad, G. P.; Steinfeld, A. Review: Photochemical and thermochemical production of solar fuels from H2O and CO2 using metal oxide catalysts. *Ind. Eng. Chem. Res.* **2012**, *51*, 11828−11840.

(3) Ackermann, S.; Sauvin, L.; Castiglioni, R.; Rupp, J. L.; Scheffe, J. R.; Steinfeld, A. Kinetics of CO2 reduction over nonstoichiometric ceria. *J. Phys. Chem. C* **2015**, *119*, 16452−16461.

(4) Chueh, W. C.; Haile, S. M. A thermochemical study of ceria: exploiting an old material for new modes of energy conversion and CO2 mitigation. *Philos. Trans. R. Soc., A* **2010**, *368*, 3269−3294.

(5) Scheffe, J. R.; Steinfeld, A. Oxygen exchange materials for solar thermochemical splitting of H2O and CO2: a review. *Mater. Today* **2014**, *17*, 341.

(6) Ackermann, S.; Scheffe, J. R.; Steinfeld, A. Diffusion of Oxygen in Ceria at Elevated Temperatures and Its Application to H2O/CO2 Splitting Thermochemical Redox Cycles. *J. Phys. Chem. C* **2014**, *118*, 5216−5225.

(7) Venstrom, L. J.; De Smith, R. M.; Hao, Y.; Haile, S. M.; Davidson, J. H. Efficient Splitting of CO2 in an Isothermal Redox Cycle based on Ceria. *Energy Fuels* **2014**, *28*, 2732.

(8) Bader, R.; Bala Chandran, R.; Venstrom, L. J.; Sedler, S. J.; Krenzke, P. T.; De Smith, R. M.; Banerjee, A.; Chase, T. R.; Davidson, J. H.; Lipiński, W. Design of a Solar Reactor to Split CO2 Via Isothermal Redox Cycling of Ceria. *J. Sol. Energy Eng.* **2015**, *137*, 031007−031007.

(9) Chueh, W. C.; Falter, C.; Abbott, M.; Scipio, D.; Furler, P.; Haile, S. M.; Steinfeld, A. High-Flux Solar-Driven Thermochemical Dissociation of CO2 and H2O Using Nonstoichiometric Ceria. *Science* **2010**, *330*, 1797−1801.

(10) Furler, P.; Scheffe, J.; Gorbar, M.; Moes, L.; Vogt, U.; Steinfeld, A. Solar Thermochemical CO2 Splitting Utilizing a Reticulated Porous Ceria Redox System. *Energy Fuels* **2012**, *26*, 7051−7059.

(11) Furler, P.; Scheffe, J. R.; Steinfeld, A. Syngas production by simultaneous splitting of H2O and CO 2 via ceria redox reactions in a high-temperature solar reactor. *Energy Environ. Sci.* **2012**, *5*, 6098−6103.

(12) Roeb, M.; Säck, J. P.; Rietbrock, P.; Prahl, C.; Schreiber, H.; Neises, M.; de Oliveira, L.; Graf, D.; Ebert, M.; Reinalter, W.; Meyer-Grünefeldt, M.; Sattler, C.; Lopez, A.; Vidal, A.; Elsberg, A.; Stobbe, P.; Jones, D.; Steele, A.; Lorentzou, S.; Pagkoura, C.; Zygogianni, A.; Agrafiotis, C.; Konstandopoulos, A. G. Test operation of a 100 kW pilot plant for solar hydrogen production from water on a solar tower. *Sol. Energy* **2011**, *85*, 634−644.

DOI: 10.1021/acs.iecr.7b02738
Ind. Eng. Chem. Res. 2017, 56, 10300−10308

(13) Marxer, D.; Furler, P.; Takacs, M.; Steinfeld, A. Solar thermochemical splitting of CO2 into separate streams of CO and O2 with high selectivity, stability, conversion, and efficiency. *Energy Environ. Sci.* **2017**, *10*, 1142.
(14) Diver, R. B.; Miller, J. E.; Allendorf, M. D.; Siegel, N. P.; Hogan, R. E. Solar Thermochemical Water-Splitting Ferrite-Cycle Heat Engines. *J. Sol. Energy Eng.* **2008**, *130*, 041001−041001−8.
(15) Lapp, J.; Davidson, J. H.; Lipiński, W. Heat Transfer Analysis of a Solid-Solid Heat Recuperation System for Solar-Driven Non-stoichiometric Redox Cycles. *J. Sol. Energy Eng.* **2013**, *135*, 031004−031004−11.
(16) Kaneko, H.; Miura, T.; Fuse, A.; Ishihara, H.; Taku, S.; Fukuzumi, H.; Naganuma, Y.; Tamaura, Y. Rotary-Type Solar Reactor for Solar Hydrogen Production with Two-step Water Splitting Process. *Energy Fuels* **2007**, *21*, 2287−2293.
(17) Scheffe, J. R.; Welte, M.; Steinfeld, A. Thermal Reduction of Ceria within an Aerosol Reactor for H2O and CO2 Splitting. *Ind. Eng. Chem. Res.* **2014**, *53*, 2175−2182.
(18) Welte, M.; Barhoumi, R.; Zbinden, A.; Scheffe, J. R.; Steinfeld, A. Experimental Demonstration of the Thermochemical Reduction of Ceria in a Solar Aerosol Reactor. *Ind. Eng. Chem. Res.* **2016**, *55*, 10618.
(19) Ermanoski, I.; Siegel, N. P.; Stechel, E. B. A New Reactor Concept for Efficient Solar-Thermochemical Fuel Production. *J. Sol. Energy Eng.* **2013**, *135*, 031002−031002.
(20) Brendelberger, S.; Sattler, C. Concept analysis of an indirect particle-based redox process for solar-driven H2O/CO2 splitting. *Sol. Energy* **2015**, *113*, 158−170.
(21) Krenzke, P. T.; Davidson, J. H. Thermodynamic Analysis of Syngas Production via the Solar Thermochemical Cerium Oxide Redox Cycle with Methane-Driven Reduction. *Energy Fuels* **2014**, *28*, 4088−4095.
(22) Warren, K. J.; Reim, J.; Randhir, K.; Greek, B.; Carrillo, R.; Hahn, D. W.; Scheffe, J. Theoretical and Experimental Investigation of Solar Methane Reforming via the Nonstoichiometric Ceria Redox Cycle. *Energy Technol.* **2017**, DOI: 10.1002/ente.201700083.
(23) Panlener, R. J.; Blumenthal, R. N.; Garnier, J. E. A thermodynamic study of nonstoichiometric cerium dioxide. *J. Phys. Chem. Solids* **1975**, *36*, 1213−1222.
(24) Takacs, M.; Scheffe, J.; Steinfeld, A. Oxygen nonstoichiometry and thermodynamic characterization of Zr doped ceria in the 1573−1773 K temperature range. *Phys. Chem. Chem. Phys.* **2015**, *17*, 7813−7822.
(25) Steinfeld, A.; Kuhn, P.; Karni, J. High-temperature solar thermochemistry: Production of iron and synthesis gas by Fe3O4-reduction with methane. *Energy* **1993**, *18*, 239−249.
(26) Steinfeld, A.; Thompson, G. Solar combined thermochemical processes for CO2 mitigation in the iron, cement, and syngas industries. *Energy* **1994**, *19*, 1077−1081.
(27) Krenzke, P. T.; Fosheim, J. R.; Zheng, J.; Davidson, J. H. Synthesis gas production via the solar partial oxidation of methane-ceria redox cycle: Conversion, selectivity, and efficiency. *Int. J. Hydrogen Energy* **2016**, *41*, 12799−12811.
(28) Otsuka, K.; Sunada, E.; Ushiyama, T.; Yamanaka, I. The production of synthesis gas by the redox of cerium oxide. *Stud. Surf. Sci. Catal.* **1997**, *107*, 531−536.
(29) Tang, M.; Xu, L.; Fan, M. Progress in oxygen carrier development of methane-based chemical-looping reforming: A review. *Appl. Energy* **2015**, *151*, 143−156.
(30) Aston, V. J.; Evanko, B. W.; Weimer, A. W. Investigation of novel mixed metal ferrites for pure H2 and CO2 production using chemical looping. *Int. J. Hydrogen Energy* **2013**, *38*, 9085−9096.
(31) Bhavsar, S.; Najera, M.; Veser, G. Chemical Looping Dry Reforming as Novel, Intensified Process for CO2 Activation. *Chem. Eng. Technol.* **2012**, *35*, 1281−1290.
(32) Kathe, M. V.; Empfield, A.; Na, J.; Blair, E.; Fan, L.-S. Hydrogen production from natural gas using an iron-based chemical looping technology: Thermodynamic simulations and process system analysis. *Appl. Energy* **2016**, *165*, 183−201.
(33) Rihko-Struckmann, L. K.; Datta, P.; Wenzel, M.; Sundmacher, K.; Dharanipragada, N.; Poelman, H.; Galvita, V. V.; Marin, G. B. Hydrogen and Carbon Monoxide Production by Chemical Looping over Iron-Aluminium Oxides. *Energy Technol.* **2016**, *4* (4), 304−313.
(34) Tong, A.; Bayham, S.; Kathe, M. V.; Zeng, L.; Luo, S.; Fan, L.-S. Iron-based syngas chemical looping process and coal-direct chemical looping process development at Ohio State University. *Appl. Energy* **2014**, *113*, 1836−1845.
(35) Sheu, E. J.; Mokheimer, E. M. A.; Ghoniem, A. F. A review of solar methane reforming systems. *Int. J. Hydrogen Energy* **2015**, *40*, 12929−12955.
(36) Zheng, R.; Diver, R.; Caldwell, D.; Fritz, B.; Cameron, R.; Humble, P.; TeGrotenhuis, W.; Dagle, R.; Wegeng, R. Integrated solar thermochemical reaction system for steam methane reforming. *Energy Procedia* **2015**, *69*, 1192−1200.
(37) Welford, W.; Winston, R. *High Collection Nonimaging Optics*; Academic Press: San Diego, 1989.
(38) Melchior, T.; Steinfeld, A. Radiative transfer within a cylindrical cavity with diffusely/specularly reflecting inner walls containing an array of tubular absorbers. *J. Sol. Energy Eng.* **2008**, *130*, 021013.
(39) Petrasch, J. r. *A Free and Open Source Monte Carlo Ray Tracing Program for Concentrating Solar Energy Research* **2010**, 125−132.
(40) Petrasch, J.; Coray, P.; Meier, A.; Brack, M.; Häberling, P.; Wuillemin, D.; Steinfeld, A. A Novel 50kW 11,000 suns High-Flux Solar Simulator Based on an Array of Xenon Arc Lamps. *J. Sol. Energy Eng.* **2007**, *129*, 405−411.

DOI: 10.1021/acs.iecr.7b02738
Ind. Eng. Chem. Res. 2017, 56, 10300−10308